Nanoscale

PAPER

View Article Online
View Journal | View Issue

Cite this: *Nanoscale*, 2025, **17**, 13366

Tailored nanoscale structure of flame-made antimony doped tin oxides and their near-infrared shielding properties†

Tung Van Pham, [a] Tomoyuki Hirano, *[a] Eishi Tanabe,[b] Eka Lutfi Septiani, [a] Kiet Le Anh Cao [a] and Takashi Ogi [a]

Today's world is confronting mounting challenges and pressures from urbanization, industrial expansion, and the effects of climate change. These forces are fueling a surge in energy consumption, placing heavy demands on our limited resources. Buildings are a key contributor to this issue, as the need for cooling, heightened by heat from sunlight streaming through windows, emphasizes the critical importance of adopting energy-efficient solutions. Near-infrared (NIR) shielding glass, which blocks NIR radiation while allowing visible light transmission, is a promising approach for reducing cooling demands. Antimony-doped tin oxide (ATO) nanoparticles, known for their high thermal stability and electrical conductivity, offer a viable solution for NIR shielding due to their localized surface plasmon resonance (LSPR) effect. In this study, we systematically investigate the influence of the nanostructure, especially the crystal/particle diameter, on the NIR shielding performance of ATO nanoparticles synthesized *via* flame spray pyrolysis (FSP). Flame-made ATO nanoparticles ranging from around 5 to 35 nm were synthesized, characterized, and evaluated for their optical properties across the UV-VIS-NIR spectrum. The results reveal a strong dependence of NIR shielding performance on the crystal/particle diameter, with ATO nanoparticles averaging 20 nm demonstrating optimal NIR absorption while maintaining high visible light transmittance. X-ray photoelectron spectroscopy analysis indicates that the Sb^{5+}/Sb^{3+} ion ratio plays a crucial role in modulating the free electron concentration and enhancing LSPR. Our findings demonstrate that precise engineering of the ATO crystal/particle diameter and composition by FSP can significantly enhance their optical performance, facilitating their application in energy-efficient smart glass technologies.

Received 16th December 2024,
Accepted 29th April 2025

DOI: 10.1039/d4nr05289g

rsc.li/nanoscale

1. Introduction

The modern world faces unprecedented challenges driven by rapid urbanization, industrial growth, and climate change. Energy consumption has soared to meet the demands of expanding populations and technological advancements, placing immense pressure on finite natural resources. In the face of mounting energy demands and escalating environmental challenges, the need for innovative solutions to enhance energy efficiency has never been more urgent.[1,2] Buildings play a pivotal role in this challenge as they are responsible for a substantial portion of energy consumption.[3] Cooling systems consume vast amounts of energy,[4,5] exacerbated by solar heat gain through windows. Near-infrared radiation (NIR), which constitutes a significant fraction of solar energy, penetrates conventional windows and causes indoor temperatures to rise, increasing the demand for air conditioning.[4,6] As energy consumption rises, so do greenhouse gas emissions, making it essential to find innovative ways to reduce heat transfer into buildings. The development of NIR shielding glass, designed to block the infrared portion of sunlight while allowing visible light to pass through, offers a promising solution to enhance energy efficiency, reduce cooling costs, and minimize environmental impacts.[7,8]

[a]*Chemical Engineering Program, Department of Advanced Science and Engineering, Graduate School of Advanced Science and Engineering, Hiroshima University, 1-4-1 Kagamiyama, Higashi-Hiroshima City, Hiroshima 739-8527, Japan. E-mail: tomoyuki-hirano@hiroshima-u.ac.jp; Tel: +81-82-424-7850; Fax: +81-82-424-7850*

[b]*Hiroshima Prefectural Institute of Industrial Science and Technology, 3-10-31 Kagamiyama, Higashi-Hiroshima City, Hiroshima 739-0046, Japan*

† Electronic supplementary information (ESI) available: Additional TEM images of flame-made ATO NPs, N_2 adsorption–desorption measurement and calculations for the average BET particle diameter (d_{BET}) of various sized ATO NPs, flame conditions for synthesizing ATO NPs and calculations for combustion enthalpy density, hydrodynamic particle size of flame-made ATO NPs by DLS measurement, wide-scan XPS spectra of the as-synthesized ATO NPs, calculations for equivalence ratios of each flame condition for synthesizing various-sized ATO NPs, normalized representation, 3D visualization of UV–VIS–NIR spectra and optical band gap calculations using the Tauc plot method for flame-made ATO NPs (5–35 nm). See DOI: https://doi.org/10.1039/d4nr05289g

To address energy consumption challenges, considerable attention has been given to integrating advanced materials such as antimony-doped tin oxide (ATO),[6,9–13] indium-doped tin oxide,[14–16] cesium-doped tungsten oxide,[17–23] and lanthanum hexaboride,[24] leveraging their optical properties – particularly NIR-shielding capabilities – to improve energy efficiency. Among these materials, ATO nanoparticles (ATO NPs) have emerged as a promising candidate due to their NIR-shielding properties,[6,12,25] high thermal stability,[26] and excellent electrical conductivity.[10] ATO NPs are n-type semiconductors with a wide bandgap, which can effectively block NIR radiation by the localized surface plasmon resonance (LSPR) effect, a phenomenon where free charge carriers (electrons) oscillate in resonance with incident electromagnetic waves, particularly at NIR frequencies. This oscillation leads to strong absorption and scattering of NIR light while maintaining high visible light transmittance.[12,13] This dual functionality is crucial for developing energy-efficient windows that can reduce the energy load for air conditioning without compromising natural lighting. Additionally, the LSPR effect is also largely dependent on the nanostructure, especially the crystal/particle diameter of the material, which determines the efficiency of the surface interaction between light and the material.[27–30] Therefore, precise engineering of the nanostructure during synthesis is crucial for achieving the high NIR-shielding performance of the ATO NPs.

In addition, aerosol processes are advanced synthesis techniques that enable the production of nanoparticles with controlled sizes,[31–33] morphologies,[34–36] and compositions.[37–42] Among these, the flame spray pyrolysis (FSP) method stands out for its efficiency and versatility in synthesizing nanoparticles with controllable size and composition, as evidenced by previous studies.[43–46] Unlike solution-phase methods, which require multiple processing steps such as precipitation, aging, washing, drying, and calcination, FSP enables a single-step, continuous gas-phase synthesis. This approach offers precise control over particle formation while significantly reducing processing time and energy consumption. In one such study, Mädler *et al.* successfully controlled the silica particle size by adjusting the oxidant and precursor fuel composition in the FSP process.[33] Additionally, the rapid quenching at high temperature during FSP enables the formation of metastable phases that are challenging to achieve through wet-chemical methods, further broadening the range of tunable material properties. For instance, Mohammadi *et al.* demonstrated FSP's versatility in controlling the composition of MnO_x nanoparticles by monitoring the high-temperature residence time of droplets.[47] Additionally, FSP stands out for its high production rates, flexibility in doping with various elements, and ability to produce nanoparticles with narrow size distribution and high purity.[48,49] These advantages make FSP a suitable method for synthesizing ATO NPs, offering enhanced NIR shielding performance alongside industrial scalability.

In this study, for the first time, we systematically investigate the effect of the crystal/particle diameter of flame-made ATO NPs on NIR-shielding performance. By synthesizing ATO NPs of varying sizes through FSP, we aim to elucidate the crystal/particle diameter that maximizes NIR absorption while ensuring high visible light transmittance. Our findings provide critical insights into the design and application of ATO-based nanomaterials for energy-efficient window technologies. The ability to fine-tune the NIR-shielding performance through nanocrystal/particle diameter engineering not only enhances the material's functionality but also broadens its applicability in various architectural and automotive contexts. This study underscores the potential of FSP as a robust and scalable method for producing high-performance NIR-shielding materials, paving the way for more energy-efficient building solutions.

2. Experimental section

2.1 Synthesis of flame-made ATO NPs

ATO NPs with various sizes were synthesized using the FSP method. The precursors for the synthesis were tin(II) 2-ethylhexanoate ($C_{16}H_{30}O_4Sn$, Sigma Aldrich) and antimony(III) ethoxide ($Sb(OC_2H_5)_3$, Sigma Aldrich), which were dissolved in xylene ($C_6H_4(CH_3)_2$, Sigma Aldrich) as the solvent. Solutions with total concentrations of tin and antimony at 0.1, 0.5, 1 or 1.2 mol L^{-1} were prepared, maintaining an antimony concentration corresponding to 10 at% of total concentrations. The 10 at% Sb was chosen to optimize NIR shielding and visible light transmittance, as higher Sb can reduce crystallinity, while lower Sb limits free electron density for plasmonic performance.[12,50] These solutions were dispensed using a syringe pump at a controlled rate (1.5–25 mL min^{-1}) and atomized using a two-fluid nozzle (model AM6, ATOMAX Co., Shizuoka, Japan) in the presence of oxygen at a flow rate of 3 or 4 L min^{-1}. Both the feed flow rate and oxygen flow rate were varied to control the crystal/particle diameter of the ATO NPs. The atomized solutions were then combusted using a premixed methane/air flame with flow rates of 1.55 L min^{-1} and 6.67 L min^{-1}, respectively. ATO NPs were collected using the glass microfiber filter (Whatman, ∅ 240 mm, Sigma Aldrich) and used for optical measurements without further purification. The prepared ATO NPs were designated as **ATO-*X***, where *X* represents the rounded crystal diameter, calculated from XRD patterns with the Scherrer equation, ranging from 5 to 35 nm.

2.2 Material characterization

The morphologies of the prepared samples were observed using transmission electron microscopy (TEM; JEM-2010, 200 kV, JEOL Corp., Japan). The elemental analysis was conducted by energy-dispersive X-ray spectroscopy (EDS) using scanning transmission electron microscopy (STEM) (JEM-3000F, 297 kV, JEOL Corp., Japan). X-ray diffraction (XRD) was conducted to investigate the crystal structure of the synthesized particles using Bruker D2 PHASER model apparatus (Billerica, Massachusetts, USA) under operating conditions at 40 kV and 30 mA. Specific surface areas (SSA) were determined from

nitrogen adsorption–desorption obtained at 77 K using a BELSORP-max instrument model with the Brunauer–Emmett–Teller (BET) method. The chemical compositions of the as-prepared products were analyzed using an X-ray photoelectron spectrometer (XPS, ESCA-3400, Shimadzu Corp., Kyoto, Japan, operating at 10 kV and 20 mA) equipped with a standard monochromatic Mg-Kα source ($h\nu$ = 1253.6 eV). The binding energy data were calibrated with respect to the C 1s signal of the ambient hydrocarbons (C–H and C–C) at 284.3 eV and the Shirley method was used for background subtraction. The hydrodynamic diameters of flame-made ATO NPs were measured using a Zetasizer Nano ZSP (Malvern Instrument Inc., London, UK). For evaluating NIR shielding performance, ATO NPs with various crystal/particle diameters were dispersed in ethanol at a concentration of 0.05 wt%. The UV-VIS-NIR transmittance spectra of dispersed solutions of ATO NPs were measured using a V-770 UV-Visible/NIR Spectrophotometer (JASCO Corp, Japan) employing quartz standard cells, T-21-UV-10 (TOSOH Corp, Japan).

3. Results and discussion

3.1 Characterization of flame-made ATO NPs

Fig. 1a illustrates the formation process of ATO NPs during flame spray pyrolysis. This synthesis technique allows for precise control of nanoparticle characteristics by adjusting various flame parameters, such as the flow rates of dispersion gas and fuels, along with the precursor concentration and feed rate.[49] These factors together enable fine-tuning of the particle diameter and composition, making FSP an efficient method for synthesizing ATO NPs with tailored properties. The TEM images of the ATO NP series synthesized *via* FSP reveal a diverse range of nanocrystal sizes, exhibiting a distinct trend of enhanced crystal/particle growth as the size progressively increases from approximately 5 to 35 nm (Fig. 1b and section 1, ESI†). This progression suggests that the FSP conditions effectively promote controlled crystal/particle growth, yielding nanoparticles with varied, yet predictable sizes. The particle diameter histograms exhibit relatively narrow geometric standard deviations (σ), highlighting the uniformity in size distribution across the samples (Fig. 1c). This consistency underscores the precision of the FSP method in controlling size distribution despite variations in size.

Furthermore, high-resolution TEM (HRTEM) images further confirm the crystalline nature of the ATO NPs, with visible lattice fringes indicating high crystallinity across different particle diameters (Fig. 1d and section 1, ESI†). This demonstrates the FSP method's effectiveness not only in controlling the particle diameter but also in preserving the structural integrity of the nanoparticles. Additionally, Fig. 1e presents a spatially resolved compositional analysis of the synthesized ATO NPs (**ATO-5**, **ATO-20**, and **ATO-35**) using STEM combined with EDS. The EDS elemental maps confirm a homogeneous distribution of antimony in both the **ATO-5** and **ATO-20** samples, regardless of the particle diameter, demonstrating effective incorporation of Sb dopants into the SnO_2 lattice. In contrast, the **ATO-35** sample exhibits uneven Sb distribution across the prepared particles. This phenomenon may be attributed to the reduced combustion efficiency at high feed rates (25 mL min^{-1}), which results in the incomplete combustion of the precursor solution. Consequently, this leads to localized Sb enrichment and non-uniform doping. Such an imbalance in Sb incorporation may affect the NIR shielding performance by altering the optical and electronic properties of the ATO NPs, underscoring the importance of carefully controlled synthesis conditions for achieving uniform dopant distribution.

To gain deeper insight into the crystalline properties of flame-made ATO NPs, XRD patterns for various sized ATO NPs were analyzed and are presented in Fig. 2a. The XRD patterns of flame-synthesized ATO NPs (**ATO-5** to **ATO-35**) correspond to the standard XRD pattern of rutile SnO_2 (COD no. 1534785). The absence of antimony species (metal Sb, Sb_2O_3, Sb_2O_5) in the XRD patterns further confirms that Sb is effectively incorporated into the SnO_2 crystal lattice, substituting for Sn to form a solid solution. At an Sb doping concentration of 10 at% in flame-synthesized ATO samples, no notable peak shifts are observed compared to the standard rutile SnO_2 pattern, due to the minimal size difference between Sn^{4+} ions (ionic radius 0.083 nm) and Sb^{5+} ions (ionic radius 0.074 nm).[51] This structural stability enables doping concentrations up to 30 at% Sb without inducing significant alterations to the overall crystal structure.[50] The increasing intensities of the XRD peaks, especially for the 110 and 101 reflections, can be attributed to the nanocrystalline nature of the synthesized ATO particles. By applying the Scherrer equation, the crystal diameter is estimated, revealing an increasing trend of the average crystal diameter across the ATO NP samples.

In addition, Fig. 2b presents the SSA of the synthesized ATO NPs obtained from nitrogen adsorption–desorption measurement at 77 K with the BET method, revealing a clear trend where the SSA decreases as the crystal/particle diameter increases, ranging from 173.00 m^2 g^{-1} for the **ATO-5** sample to 24.02 m^2 g^{-1} for the **ATO-35** sample. This observation aligns with the fundamental principle that smaller particles possess a larger surface area relative to their volume, as they expose more surface atoms or molecules. In contrast, as the particles grow larger, their surface-to-volume ratio diminishes, leading to the corresponding reduction in SSA. Additionally, from nitrogen adsorption–desorption measurements and SSA values, the average BET particle diameter of ATO NPs can be calculated, assuming the particles are spherical and free from aggregation or sintering (Fig. 2b and section S2, ESI†). In terms of the LSPR effect, both the size and SSA play critical roles in determining the NIR shielding performance, which will be further discussed later. Additionally, through the investigation of flame conditions and the subsequent calculations, the exponential relationship between the combustion enthalpy density and the crystal diameter (d_c), particle diameter (d_p) and average BET diameter (d_{BET}) of ATO NPs is illustrated in Fig. 2c. Detailed calculations for d_{BET} and flame conditions for

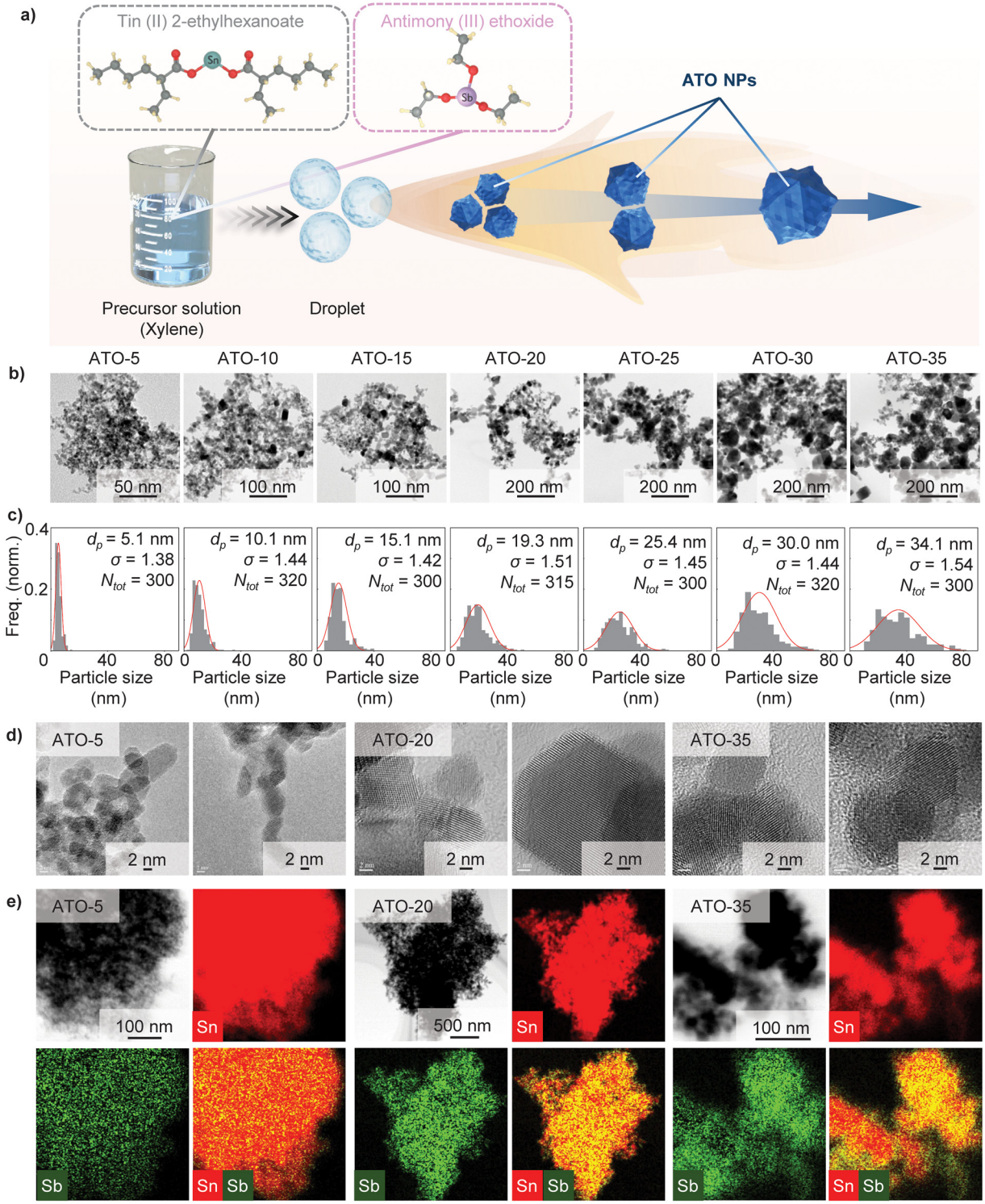

Fig. 1 (a) Schematic of crystal/particle growth of ATO NPs in the FSP process. (b) TEM images of ATO NPs with various particle diameters (approximately 5–35 nm). (c) Histograms of particle diameter distribution, measured from at least 300 nanoparticle diameters using TEM images of each ATO NP sample. d_p, σ and N_{tot} values represent the geometric mean, geometric standard deviation, and number of measured particles, respectively. (d) HRTEM images depicting the crystalline nature of **ATO-5**, **ATO-20** and **ATO-35** and (e) their STEM–EDS elemental maps for Sn, Sb, and combined Sn/Sb (calculated based on peak analysis, ROI at%, and noise consideration).

the as-synthesized ATO NPs are provided in section S3 (ESI†). The result further demonstrates the potential for predicting synthesized crystal/particle diameters based on flame conditions of FSP. The minimal difference observed between d_p and d_c, ranging from 0.8 to 6.3% across the synthesized ATO NPs (Fig. 2c), strongly suggests that these ATO NPs exist predo-

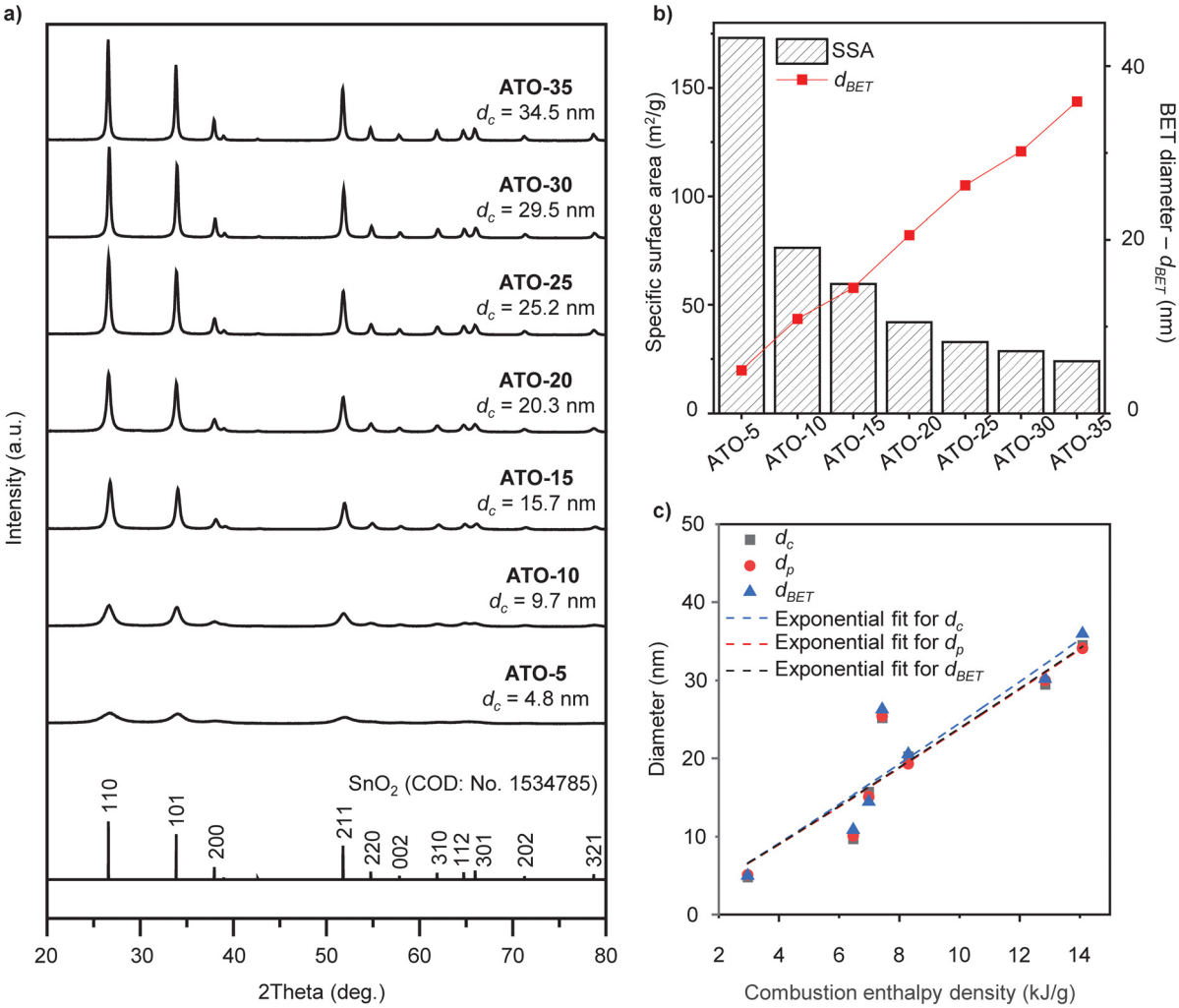

Fig. 2 (a) XRD patterns of variously sized ATO NPs ranging from 4.8 to 34.5 nm, (b) the SSA of all flame-made ATO NPs and (c) the relationship between the crystal diameter (d_c), particle diameter (d_p) or average BET diameter (d_{BET}) of the prepared samples and the combustion enthalpy density of flame conditions.

minantly as single crystals instead of polycrystalline structures. The largest observed discrepancy, found in the **ATO-5** sample with the smallest particle diameter, remains within a negligible range, further supporting the conclusion of monocrystalline morphology. In polycrystalline nanoparticles, a more significant discrepancy between particle and crystal diameters is typically expected due to the presence of grain boundaries and multiple crystalline domains within each particle. Therefore, the consistent alignment of particle and crystal dimensions across various samples synthesized *via* FSP highlights the predominance of single-crystalline characteristics in these ATO NPs, which may enhance their structural stability and uniformity in electronic and optical properties. The observation that d_{BET} values are consistently larger than d_c for most of the synthesized ATO samples, with only minimal differences ranging from 1.4% to 12.3% (highest in the **ATO-10** sample), suggests limited occurrence of aggregation and sintering during the flame synthesis process. This suggests that the synthesis conditions employed in FSP are effective in minimizing particle aggregation and maintaining non-aggregated ATO NPs, enhancing their utility for applications requiring high surface area and stability. Besides that, the hydrodynamic diameters (d_h) of various sized ATO NPs were also provided and are discussed in section S4, ESI.† The obtained results from DLS measurement reveal the increasing trend of d_h with other dimension parameters (d_p, d_c and d_{BET}). While **ATO-5** to **ATO-25** exhibit a gradual size increase, a significant jump is observed for **ATO-30** (357.85 nm) and **ATO-35** (415.53 nm), indicating enhanced agglomeration. This deviation can be attributed to stronger interparticle interactions, as larger particles experience reduced specific surface area while increasing van der Waals forces, leading to clustering in dispersion. Furthermore, FSP synthesis conditions influence particle interactions, as larger ATO NPs undergo higher collision rates during synthesis, promoting the formation of soft agglomerates. These factors contribute to the large hydrodynamic sizes in DLS measurements.

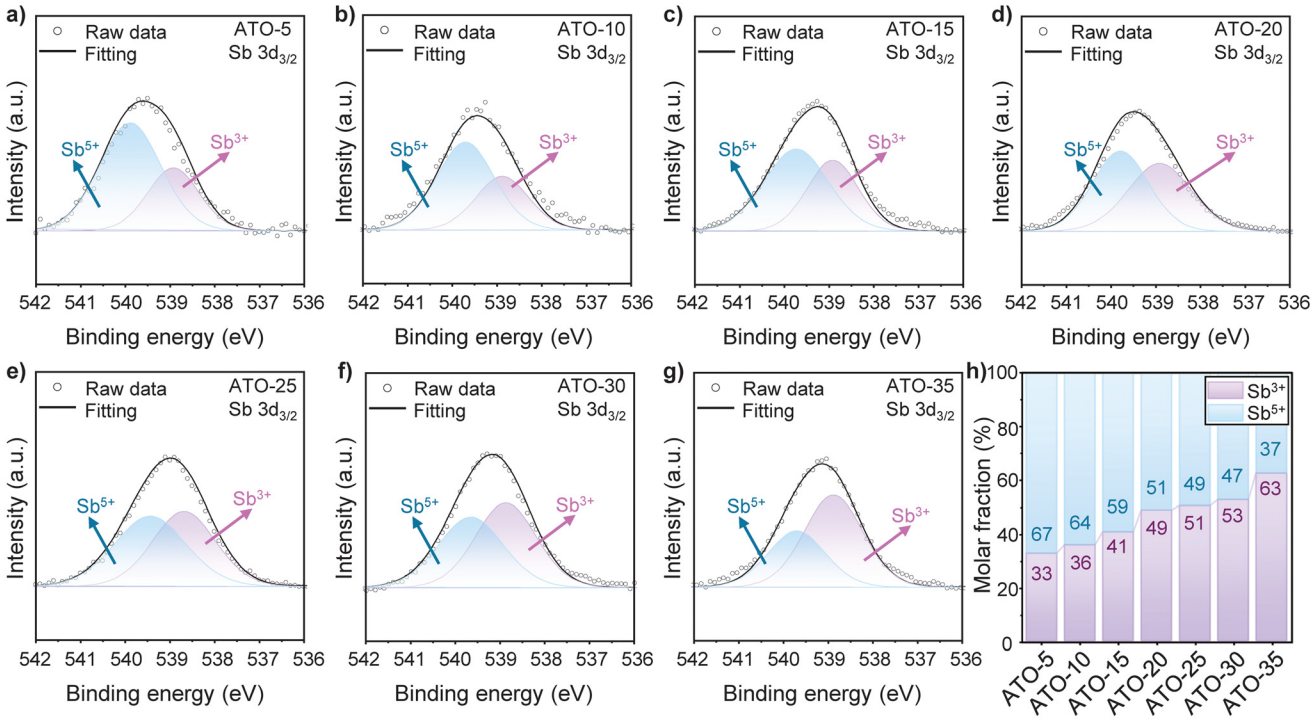

Fig. 3 XPS spectra for Sb $3d_{3/2}$ of the various sized ATO NPs (a–g) **ATO-5** to **ATO-35** and (h) Sb^{3+}/Sb^{5+} ratios obtained by deconvoluting the peak of Sb $3d_{3/2}$ of the prepared samples.

XPS measurements were conducted to further investigate the chemical composition and antimony valence states of the prepared ATO NPs. The wide-scan XPS spectra of the as-prepared ATO nanoparticles revealed peaks corresponding to Sn, Sb, O, and C, providing additional confirmation that the Sb element was successfully incorporated into the crystal structure (section S5, ESI†). Fig. 3a–g depict the results of the Sb $3d_{3/2}$ peak within the range of 536–542 eV. The data revealed the coexistence of two valence states of Sb in all flame-made ATO NPs. Through deconvolution of the Sb $3d_{3/2}$ curve, two distinct peaks at around 538.9 and 539.8 eV were identified, corresponding to Sb^{3+} and Sb^{5+} ions, respectively.[6,52] The results further indicate significant differences in the Sb^{3+}/Sb^{5+} ratios among the variously sized ATO NPs, as shown in Fig. 3h. Specifically, the Sb^{5+} ion fraction reaches 67% in the **ATO-5** sample, gradually decreasing as the crystal/particle diameter increases. This trend can be explained by the variation in the equivalence ratio ($\dot{\Phi}$) under different synthesis conditions, when controlling the nanoscale size of ATO NPs (ranging from 5 to 35 nm). Detailed calculations of the equivalence ratio for each flame condition are presented in section S6 (ESI†). To synthesize larger sizes of ATO NPs, modified synthesis conditions with a higher precursor feed rate resulted in a corresponding increase in the $\dot{\Phi}$ value. Beginning with a $\dot{\Phi}$ value of 0.44 for the smallest size ATO NPs (**ATO-5**), indicating fuel-lean conditions under which the fuel undergoes complete oxidation, the ratio progressively increases, reaching a highest value of 6.75 in **ATO-35**, which reflects fuel-rich conditions characterized by a deficiency of an oxidative agent in the combustion process. This lack of oxidation potential in the fuel-rich environment hinders the oxidation of Sb^{3+} to Sb^{5+}, resulting in an increasing Sb^{3+}/Sb^{5+} ratio as the size grows. The optical properties of the as-synthesized ATO NPs, particularly their NIR shielding performance, are significantly influenced by their electrical characteristics.[25] Among the two valence states of antimony present in ATO NPs, Sb^{3+} ions act as electron acceptors, while Sb^{5+} ions serve as electron donors, directly affecting the concentration of free electrons of the material. Consequently, when both valence states coexist, their opposing effects can partially neutralize each other, which can be considered to explain their optical performances. When n-doping is predominantly driven by Sb^{5+} ions, a higher concentration of free electrons is contributed to the conduction band, leading to an enhancement of the LSPR effect of the synthesized material.[25] This, in turn, results in strong NIR shielding performance. Conversely, when Sb^{3+} ions dominate, the NIR shielding performance is significantly reduced.

3.2 Evaluating NIR shielding performance

To further investigate the optical performance of the synthesized ATO NP samples with varying sizes, UV–VIS–NIR spectra (covering the spectral range of 200–2000 nm) were measured for 0.05 wt% ATO NP solutions, with ethanol used as the blank reference, as shown in Fig. 4a. Furthermore, the normalized spectra and 3D visualization of UV-VIS-NIR spectra are presented in Fig. S6 (ESI†). The obtained results demon-

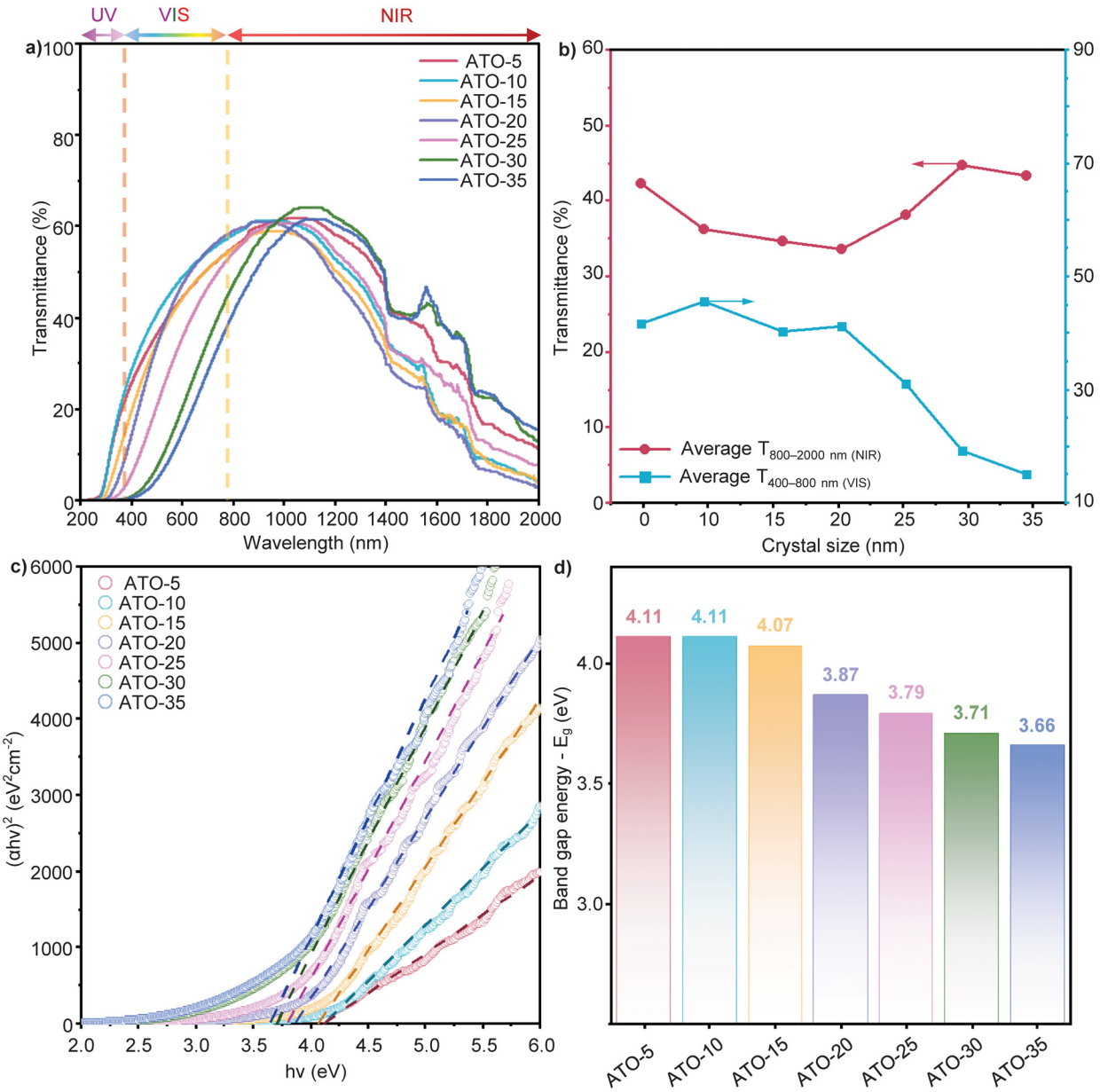

Fig. 4 (a) UV–VIS–NIR spectra of flame-made ATO NPs with various crystal/particle diameters (around 5–35 nm) and (b) their average transmittance in the UV and NIR ranges. (c) Tauc plot for determining the optical band gap (E_g) of the as-synthesized ATO NPs and (d) the obtained band gap value.

strate shifts in the UV–VIS–NIR spectra of various sized ATO NPs, indicating that the optical properties of these nanoparticles are dependent on their size across the UV, visible, and NIR wavelength ranges. This spectral dependence highlights the influence of nano size on light absorption and scattering characteristics within the synthesized ATO NPs. As shown in Fig. 4b and Table S5 (ESI†), in the UV region (200–380 nm), an increase in blocking performance is observed as the ATO NP size grows, with **ATO-35** blocking up to 99.95% of UV light, compared to 92.66% for **ATO-5**. This enhancement is attributed to the larger particles having enhanced light scattering ability, which leads to improved blocking performance of UV photons.[53] In the visible range, smaller ATO NPs (5–15 nm) exhibit higher transmittance, maintaining levels above 40%. In contrast, as the crystal/particle diameter increases (20–35 nm), visible transmittance decreases significantly, with the **ATO-35** sample showing only 15.09% transmittance. This suggests that smaller particles offer better transparency in the visible range, while larger particles tend to have higher blocking performance due to increased scattering and absorption. Furthermore, the relationship between NIR transmittance and ATO NP size is shown in Fig. 4b. The NIR transmittance (T_{NIR}) decreases progressively from 42.26% to 33.61% as the crystal/particle dia-

meter increases from 5 to 20 nm, indicating improvements in NIR shielding performances in this size range. However, as the crystal/particle diameter increases further (from 20 to 35 nm), a reduction in NIR shielding efficiency is observed, suggesting a diminishing ability to block NIR radiation in larger particles. Based on the optical properties of the ATO NP series, it is evident that the **ATO-20** sample exhibits the highest NIR performance while maintaining high visible transmittance, making it suitable for smart window applications.

The band gap energy (E_g) of ATO NPs with sizes ranging from 5 to 35 nm was determined from the UV-VIS-NIR spectra using the Tauc plot method. Based on the calculated E_g values, the electrical properties of flame-made ATO NPs were analyzed to evaluate their variation trends, with detailed calculations provided in section 7 (ESI†). Fig. 4c and d present the linear fitting results from Tauc plots for various samples and the corresponding E_g values. The results indicate a gradual decrease in E_g with increasing crystal/particle size, from 4.30 eV for **ATO-5** to 3.67 eV for **ATO-35**. This trend can be attributed to quantum confinement effects, which are more pronounced in smaller nanoparticles. For the smallest particles (**ATO-5**), the band gap is significantly wider than that of bulk SnO_2 (~3.6 eV) due to strong quantum confinement. As the particle size increases, the band gap gradually narrows, approaching values closer to that of bulk ATO. The **ATO-20** sample, with a band gap of 3.87 eV, represents a transition point where quantum confinement effects begin to diminish. Furthermore, the influence of band gap energy variations

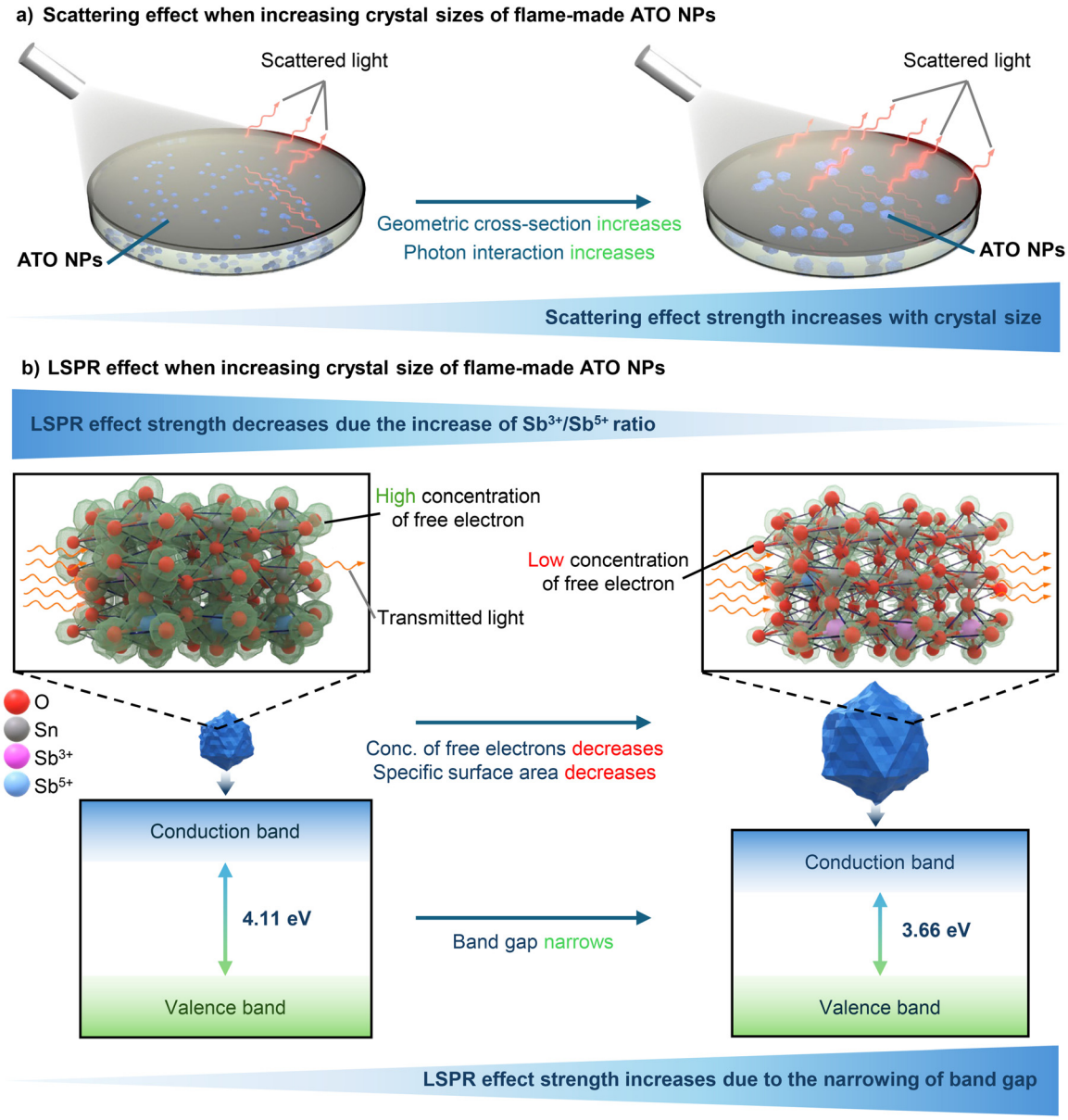

Fig. 5 Illustration for trends of (a) the scattering effect strength and (b) the LSPR effect strength corresponding to the crystal/particle diameter of ATO NPs in the NIR region.

across different ATO NP sizes on the LSPR effect and NIR shielding performance will be discussed in greater detail in the following section.

Furthermore, these optical shielding performances can be generally explained by the combined effects of light scattering and LSPR, both of which are significantly influenced by the ATO NP size. In the visible light region, the influence of light scattering is more pronounced than that of LSPR due to the nanoparticle size relative to the wavelength of visible light. For smaller particles, light scattering is minimized, allowing more visible light to pass through, whereas larger particles scatter light more effectively.[53,54] As a result, the light scattering effect intensifies with increasing ATO NP size, leading to reduced visible light transmittance.

In contrast, in the NIR range, the optical performance is governed by both the light scattering effect and the LSPR effect, as illustrated in Fig. 5. Here, the light scattering effect also tends to increase with the size of ATO NPs, enhancing NIR shielding performance due to the increase of the cross-section diameter for producing stronger scattered light signals at different angles, which results from their increased interaction with the light field (Fig. 5a).[53]

While the light scattering effect enhances NIR shielding performance as the ATO NP size increases, the influence of the LSPR effect exhibits a more complex interplay between free electron concentrations and band gap energy, as illustrated in Fig. 5b. Specifically, the Sb^{3+}/Sb^{5+} ratio increases with the ATO NP size, leading to a reduction in free electrons available for plasmonic excitation. Moreover, the concurrent decrease in SSA further limits the surface-active sizes for free electrons, collectively weakening the LSPR effect as the dimensional parameter of ATO NPs increases. Conversely, the calculated E_g follows a narrowing trend with increasing nanoparticle size (Fig. 4d), facilitating electron promotion to the conduction band and thereby enhancing the LSPR effect. This competing influence introduces a trade-off in the LSPR effect strength. Smaller particles, such as **ATO-5**, benefit from an abundance of free electrons due to the predominance of Sb^{5+} species; however, their wider band gap (4.11 eV) restricts electron excitation, ultimately limiting the LSPR effect. In contrast, while larger particles, such as **ATO-35**, exhibit a narrower band gap (3.66 eV), the predominance of Sb^{3+} species leads to a reduction in free electron availability, thereby also weakening the LSPR effect.

Considering the combined influence of both light scattering and the LSPR effect, the optical shielding performance of ATO NPs is dictated by the interplay between these two mechanisms, both of which are size-dependent. In the NIR region, light scattering is significantly enhanced as the particle size increases due to the larger interaction cross-section with incident light, improving NIR shielding efficiency. However, excessive particle growth reduces the SSA and alters the Sb^{3+}/Sb^{5+} ratio, lowering the free electron concentration and diminishing the LSPR effect despite the concurrent band gap narrowing. As a result, **ATO-20** emerges as the optimal composition, where the synergistic contributions of light scattering and LSPR are maximized. At this intermediate particle size, light scattering is sufficiently strong to enhance NIR shielding, while the Sb^{3+}/Sb^{5+} ratio and band gap width are balanced to maintain effective plasmonic resonance.

4. Conclusions

In conclusion, this study systematically investigated the effects of nanoscale properties (crystal/particle diameter and SSA) on the NIR shielding performance of flame-made ATO NPs. The results reveal that the optical performance of ATO NPs is highly dependent on their size due to the combined effects of light scattering and LSPR. In the visible range, light scattering is the dominant factor, with larger particles scattering light more effectively and reducing transmittance. In the NIR range, both light scattering and LSPR influence shielding performance. The light scattering effect increases with the dimensional parameters of ATO NPs, enhancing NIR shielding efficiency due to the larger cross-sectional area for light interaction. However, LSPR experiences complex behavior, influenced by the size-dependent variations of the Sb^{3+}/Sb^{5+} ratio, SSA, and band gap energy. In the case of smaller particles, such as **ATO-5**, they benefit from higher free electron concentrations but face limitations due to a wider band gap. In contrast, larger ATO NPs, such as **ATO-35**, exhibit narrower band gaps but suffer from reduced free electron availability due to the higher proportion of Sb^{3+} species. The optimal NIR shielding performance is observed in **ATO-20**, where the effects of light scattering and LSPR are maximized. At this intermediate size, both the light scattering and LSPR mechanisms are balanced, resulting in efficient NIR shielding. These findings provide valuable insights into tailoring the crystal/particle diameter of flame-made ATO NPs for specific applications in energy-efficient coatings, smart windows, and other light management technologies. However, to further validate these findings and assess the practical applicability of ATO NPs in real-world scenarios, follow-up experiments will be conducted to evaluate their NIR shielding effectiveness in functional coatings and smart window applications. Specifically, ATO NP-based films and coatings will be fabricated and subjected to spectroscopic and thermal measurements to quantify their NIR absorption and heat-blocking capabilities under simulated sunlight. Additionally, the influence of the ATO NP concentration and dispersion within polymer matrices on NIR shielding performance will be investigated to optimize material formulations for potential industrial applications. These future studies will provide essential insights into the practical implementation of flame-made ATO NPs for energy-efficient coatings and light management technologies, addressing their role in mitigating climate change and global warming.

Author contributions

The manuscript was written through the contributions of all authors. All authors have given their approval to the final version of the manuscript.

Data availability

The data supporting this article have been included as part of the ESI.†

Conflicts of interest

The authors declare no conflict of interest.

Acknowledgements

This work was supported by JSPS KAKENHI Grant Number JP23H01745, JP22K20482, and JP23K13590. This work was partly supported by the Hosokawa Powder Technology Foundation, Tanikawa Foundation and Iwatani Naoji Foundation. This work was also partly supported by JST, ACT-X Grant Number JPMJAX24DG, Japan. The authors thank the Natural Science Center for Basic Research and Development (N-BARD) for access to TEM facilities.

References

1 D. Zhang, M. Zhao, Y. Wang, S. A. Vigne and R. Benkraiem, Technological Innovation and Its Influence on Energy Risk Management: Unpacking China's Energy Consumption Structure Optimisation amidst Climate Change, *Energy Econ.*, 2024, **131**, 107321, DOI: **10.1016/j.eneco.2024.107321**.

2 J. Baxter, Z. Bian, G. Chen, D. Danielson, M. S. Dresselhaus, A. G. Fedorov, T. S. Fisher, C. W. Jones, E. Maginn, U. Kortshagen, A. Manthiram, A. Nozik, D. R. Rolison, T. Sands, L. Shi, D. Sholl and Y. Wu, Nanoscale Design to Enable the Revolution in Renewable Energy, *Energy Environ. Sci.*, 2009, **2**(6), 559, DOI: **10.1039/b821698c**.

3 A. M. Omer, Energy, Environment and Sustainable Development, *Renewable Sustainable Energy Rev.*, 2008, **12**(9), 2265–2300, DOI: **10.1016/j.rser.2007.05.001**.

4 H. Khandelwal, A. P. H. J. Schenning and M. G. Debije, Infrared Regulating Smart Window Based on Organic Materials, *Adv. Energy Mater.*, 2017, **7**(14), 1602209, DOI: **10.1002/aenm.201602209**.

5 L. Yang, H. Yan and J. C. Lam, Thermal Comfort and Building Energy Consumption Implications – A Review, *Appl. Energy*, 2014, **115**, 164–173, DOI: **10.1016/j.apenergy.2013.10.062**.

6 Z. Yang, M. Zhang, X. Zhao, R. Hu, H. Zhao, S. Zeb, W. Jiang, T. Liu and X. Jiang, Fluorine-Doped ATO NCs with Enhanced LSPR Effect for Smart Windows with Adaptive Solar Modulation, *Ceram. Int.*, 2024, **50**(11), 19543–19551, DOI: **10.1016/j.ceramint.2024.03.063**.

7 J. Pu, C. Shen, J. Wang, Y. Zhang, C. Zhang and S. A. Kalogirou, Near-Infrared Absorbing Glazing for Energy-Efficient Windows: A Critical Review and Performance Assessments from the Building Requirements, *Nano Energy*, 2023, **110**, 108334, DOI: **10.1016/j.nanoen.2023.108334**.

8 M. Wu, Y. Shi, R. Li and P. Wang, Spectrally Selective Smart Window with High Near-Infrared Light Shielding and Controllable Visible Light Transmittance, *ACS Appl. Mater. Interfaces*, 2018, **10**(46), 39819–39827, DOI: **10.1021/acsami.8b15574**.

9 Y. Li, J. Liu, J. Liang, X. Yu and D. Li, Tunable Solar-Heat Shielding Property of Transparent Films Based on Mesoporous Sb-Doped SnO_2 Microspheres, *ACS Appl. Mater. Interfaces*, 2015, **7**(12), 6574–6583, DOI: **10.1021/am508711p**.

10 S. D. Ponja, B. A. D. Williamson, S. Sathasivam, D. O. Scanlon, I. P. Parkin and C. J. Carmalt, Enhanced Electrical Properties of Antimony Doped Tin Oxide Thin Films Deposited *via* Aerosol Assisted Chemical Vapour Deposition, *J. Mater. Chem. C*, 2018, **6**(27), 7257–7266, DOI: **10.1039/C8TC01929K**.

11 M. Wang, Y. Xu, Y. Liu, W. Wu and S. Xu, Synthesis of Sb-Doped SnO_2 (ATO) Hollow Microspheres and Its Application in Photo-Thermal Shielding Coating, *Prog. Org. Coat.*, 2019, **136**, 105229, DOI: **10.1016/j.porgcoat.2019.105229**.

12 Z. Yang, M. Zhang, X. Zhao, Z. Guo, S. Zeb, W. Jiang, T. Liu, R. Hu and X. Jiang, Ammonia Induced Strong LSPR Effect of Chain-like ATO Nanocrystals for Hyperspectral Selective Energy-Saving Window Applications, *Chem. Eng. J.*, 2024, **479**, 147442, DOI: **10.1016/j.cej.2023.147442**.

13 B. Shen, Y. Wang, L. Lu and H. Yang, Synthesis and Characterization of Sb-Doped SnO_2 with High Near-Infrared Shielding Property for Energy-Efficient Windows by a Facile Dual-Titration Co-Precipitation Method, *Ceram. Int.*, 2020, **46**(11), 18518–18525, DOI: **10.1016/j.ceramint.2020.04.157**.

14 K. Katagiri, R. Takabatake and K. Inumaru, Robust Infrared-Shielding Coating Films Prepared Using Perhydropolysilazane and Hydrophobized Indium Tin Oxide Nanoparticles with Tuned Surface Plasmon Resonance, *ACS Appl. Mater. Interfaces*, 2013, **5**(20), 10240–10245, DOI: **10.1021/am403011t**.

15 K. P. Sibin, G. Srinivas, H. D. Shashikala, A. Dey, N. Sridhara, A. Kumar Sharma and H. C. Barshilia, Highly Transparent and Conducting ITO/Ag/ITO Multilayer Thin Films on FEP Substrates for Flexible Electronics Applications, *Sol. Energy Mater. Sol. Cells*, 2017, **172**, 277–284, DOI: **10.1016/j.solmat.2017.08.001**.

16 T. Ogi, F. Iskandar, Y. Itoh and K. Okuyama, Characterization of Dip-Coated ITO Films Derived from Nanoparticles Synthesized by Low-Pressure Spray Pyrolysis, *J. Nanopart. Res.*, 2006, **8**(3–4), 343–350, DOI: **10.1007/s11051-005-9006-0**.

17 T. Hirano, S. Nakakura, F. G. Rinaldi, E. Tanabe, W.-N. Wang and T. Ogi, Synthesis of Highly Crystalline Hexagonal Cesium Tungsten Bronze Nanoparticles by Flame-Assisted Spray Pyrolysis, *Adv. Powder Technol.*, 2018, **29**(10), 2512–2520, DOI: **10.1016/j.apt.2018.07.001**.

18 T. M. Mattox, A. Bergerud, A. Agrawal and D. J. Milliron, Influence of Shape on the Surface Plasmon Resonance of Tungsten Bronze Nanocrystals, *Chem. Mater.*, 2014, **26**(5), 1779–1784, DOI: **10.1021/cm4030638**.

19 Q. Wang, C. Li, W. Xu, X. Zhao, J. Zhu, H. Jiang, L. Kang and Z. Zhao, Effects of Mo-Doping on Microstructure and Near-Infrared Shielding Performance of Hydrothermally Prepared Tungsten Bronzes, *Appl. Surf. Sci.*, 2017, **399**, 41–47, DOI: **10.1016/j.apsusc.2016.12.022**.

20 S. Nakakura and T. Ogi, Hexagonal Cesium Tungsten Bronze Nanoparticles Produced by Solvent-Free Spray Pyrolysis and Their near Infrared Absorption Properties, *J. Mater. Chem. C*, 2021, **9**(25), 8037–8042, DOI: **10.1039/D1TC01455B**.

21 C. Guo, S. Yin, Q. Dong and T. Sato, Simple Route to $(NH_4)_xWO_3$ Nanorods for near Infrared Absorption, *Nanoscale*, 2012, **4**(11), 3394, DOI: **10.1039/c2nr30612c**.

22 X. Wu, S. Yin, D. Xue, S. Komarneni and T. Sato, A Cs_xWO_3/ZnO Nanocomposite as a Smart Coating for Photocatalytic Environmental Cleanup and Heat Insulation, *Nanoscale*, 2015, **7**(40), 17048–17054, DOI: **10.1039/C5NR04452A**.

23 Y. Wang, Z. Yan, M. Zhang, Z. Zhang, T. Li, M. Chen and W. Dong, Flexible Core–Shell Cs_xWO_3-Based Films with High UV/NIR Filtration Efficiency and Stability, *Nanoscale Adv.*, 2021, **3**(11), 3177–3183, DOI: **10.1039/D1NA00113B**.

24 H. Takeda, H. Kuno and K. Adachi, Solar Control Dispersions and Coatings With Rare–Earth Hexaboride Nanoparticles, *J. Am. Ceram. Soc.*, 2008, **91**(9), 2897–2902, DOI: **10.1111/j.1551-2916.2008.02512.x**.

25 B. Shen, Y. Wang, L. Lu and H. Yang, PH-Dependent Doping Level and, Optical Performance of Antimony-Doped Tin Oxide Nanocrystals as Nanofillers of Spectrally Selective Coating for Energy-Efficient Windows, *Ceram. Int.*, 2021, **47**(14), 20335–20340, DOI: **10.1016/j.ceramint.2021.04.041**.

26 J. Montero, C. Guillén and J. Herrero, Nanocrystalline Antimony Doped Tin Oxide (ATO) Thin Films: A Thermal Restructuring Study, *Surf. Coat. Technol.*, 2012, **211**, 37–40, DOI: **10.1016/j.surfcoat.2011.07.068**.

27 S. Lv, Y. Du, F. Wu, Y. Cai and T. Zhou, Review on LSPR Assisted Photocatalysis: Effects of Physical Fields and Opportunities in Multifield Decoupling, *Nanoscale Adv.*, 2022, **4**(12), 2608–2631, DOI: **10.1039/D2NA00140C**.

28 X. Yue, J. Hou, H. Zhao, P. Wu, Y. Guo, Q. Shi, L. Chen, S. Peng, Z. Liu and G. Cao, Au–Ag Alloy Nanoparticles with Tunable Cavity for Plasmon-Enhanced Photocatalytic H_2 Evolution, *J. Energy Chem.*, 2020, **49**, 1–7, DOI: **10.1016/j.jechem.2020.01.005**.

29 K. L. Kelly, E. Coronado, L. L. Zhao and G. C. Schatz, The Optical Properties of Metal Nanoparticles: The Influence of Size, Shape, and Dielectric Environment, *J. Phys. Chem. B*, 2003, **107**(3), 668–677, DOI: **10.1021/jp026731y**.

30 F. Zhao, J. Zeng, M. M. Parvez Arnob, P. Sun, J. Qi, P. Motwani, M. Gheewala, C.-H. Li, A. Paterson, U. Strych, B. Raja, R. C. Willson, J. C. Wolfe, T. R. Lee and W.-C. Shih, Monolithic NPG Nanoparticles with Large Surface Area, Tunable Plasmonics, and High-Density Internal Hot-Spots, *Nanoscale*, 2014, **6**(14), 8199–8207, DOI: **10.1039/C4NR01645A**.

31 T. T. N. Ho, T. Hirano, R. Narui, H. Tsutsumi, M. Kishi, Y. Yoshikawa, K. L. A. Cao and T. Ogi, Flame-Made Ir–IrO_2/TiO_2 Particles as Anode Catalyst Support for Improved Durability in Polymer Electrolyte Fuel Cells, *ACS Appl. Energy Mater.*, 2023, **6**(11), 6064–6071, DOI: **10.1021/acsaem.3c00536**.

32 W. Y. Teoh, R. Amal and L. Mädler, Flame Spray Pyrolysis: An Enabling Technology for Nanoparticles Design and Fabrication, *Nanoscale*, 2010, **2**(8), 1324–1347, DOI: **10.1039/C0NR00017E**.

33 L. Mädler, H. K. Kammler, R. Mueller and S. E. Pratsinis, Controlled Synthesis of Nanostructured Particles by Flame Spray Pyrolysis, *J. Aerosol Sci.*, 2002, **33**(2), 369–389, DOI: **10.1016/S0021-8502(01)00159-8**.

34 T. Van Pham, T. Hirano, K. L. A. Cao, E. L. Septiani, E. Tanabe and T. Ogi, Facilitating Gas Accessibility via Macropore Engineering in Amine-Loaded Silica Particles for Enhanced CO_2 Adsorption Performance, *Energy Fuels*, 2024, **38**(17), 16743–16755, DOI: **10.1021/acs.energyfuels.4c02937**.

35 P. H. Le, S. Yamashita, K. L. A. Cao, T. Hirano, N. Tsunoji, D. B. Kautsar and T. Ogi, CO Oxidation Enabled by Three-Way Catalysts Comprising Pd/Rh Nanoparticles Supported on Al_2O_3 and $CeZrO_4$ Confined in Macroporous Polystyrene Latex Templates, *ACS Appl. Nano Mater.*, 2023, **6**(18), 17324–17335, DOI: **10.1021/acsanm.3c03954**.

36 J.-S. Park, J. K. Kim, J. H. Hong, J. S. Cho, S.-K. Park and Y. C. Kang, Advances in the Synthesis and Design of Nanostructured Materials by Aerosol Spray Processes for Efficient Energy Storage, *Nanoscale*, 2019, **11**(41), 19012–19057, DOI: **10.1039/C9NR05575D**.

37 T. Ogi, A. B. D. Nandiyanto and K. Okuyama, Nanostructuring Strategies in Functional Fine-Particle Synthesis towards Resource and Energy Saving Applications, *Adv. Powder Technol.*, 2014, **25**(1), 3–17, DOI: **10.1016/j.apt.2013.11.005**.

38 S. Wintzheimer, L. Luthardt, K. L. A. Cao, I. Imaz, D. Maspoch, T. Ogi, A. Bück, D. P. Debecker, M. Faustini and K. Mandel, Multifunctional, Hybrid Materials Design via Spray–Drying: Much More than Just Drying, *Adv. Mater.*, 2023, **35**(47), 2306648, DOI: **10.1002/adma.202306648**.

39 L. Gradon, R. Balgis, T. Hirano, A. M. Rahmatika, T. Ogi and K. Okuyama, Advanced Aerosol Technologies towards Structure and Morphologically Controlled Next-Generation Catalytic Materials, *J. Aerosol Sci.*, 2020, **149**, 105608, DOI: **10.1016/j.jaerosci.2020.105608**.

40 E. L. Septiani and T. Ogi, Advances in Aerosol Nanostructuring: Functions and Control of Next-Generation Particles, *Langmuir*, 2024, **40**(51), 26789–26799, DOI: **10.1021/acs.langmuir.4c02867**.

41 K. L. A. Cao and T. Ogi, Advanced Carbon Sphere-Based Hybrid Materials Produced by Innovative Aerosol Process

for High-Efficiency Rechargeable Batteries, *Energy Storage Mater.*, 2024, 103901, DOI: 10.1016/j.ensm.2024.103901.

42 T. Hirano, S. Kaseda, K. Le Anh Cao, F. Iskandar, E. Tanabe and T. Ogi, Multiple ZnO Core Nanoparticles Embedded in TiO_2 Nanoparticles as Agents for Acid Resistance and UV Protection, *ACS Appl. Nano Mater.*, 2022, **5**(10), 15449–15456, DOI: 10.1021/acsanm.2c03489.

43 T. Hirano, T. Tsuboi, E. Tanabe and T. Ogi, *In situ* Flame Deposition of Pt Catalysts on Nb-Doped SnO_2 Nanoparticles, *J. Alloys Compd.*, 2022, **898**, 162749, DOI: 10.1016/j.jallcom.2021.162749.

44 T. Hirano, T. Tsuboi, K. L. A. Cao, E. Tanabe and T. Ogi, High Specific Surface Area Niobium-Doped Tin Oxide Nanoparticles Produced in Spray Flames as Catalyst Supports in Polymer Electrolyte Fuel Cells, *J. Nanopart. Res.*, 2023, **25**(1), 1, DOI: 10.1007/s11051-022-05649-3.

45 T. Hirano, T. Tsuboi, T. T. N. Ho, E. Tanabe, A. Takano, M. Kataoka and T. Ogi, Porosity Engineering of Pt-Loaded Nb-SnO_2 Catalyst Layers in Polymer Electrolyte Fuel Cells, *ACS Appl. Energy Mater.*, 2023, **6**(24), 12364–12370, DOI: 10.1021/acsaem.3c02165.

46 T. Hirano, T. Tsuboi, T. T. N. Ho, E. Tanabe, A. Takano, M. Kataoka and T. Ogi, Macroporous Structures of Nb–SnO_2 Particles as a Catalyst Support Induce High Porosity and Performance in Polymer Electrolyte Fuel Cell Catalyst Layers, *Nano Lett.*, 2024, **24**(34), 10426–10433, DOI: 10.1021/acs.nanolett.4c01150.

47 S. Mohammadi, J. Poostforooshan, M. F. B. Stodt, V. Olszok, J. Kiefer, U. Fritsching and A. P. Weber, Tailoring Crystal Structure and Morphology of MnO_x Nanoparticles via Electrospray-Assisted Flame Spray Pyrolysis, *Appl. Energy Combust. Sci.*, 2023, **14**, 100151, DOI: 10.1016/j.jaecs.2023.100151.

48 Z. U. Abideen, W. U. Arifeen and A. Tricoli, Advances in Flame Synthesis of Nano-Scale Architectures for Chemical, Biomolecular, Plasmonic, and Light Sensing, *Nanoscale*, 2024, **16**(16), 7752–7785, DOI: 10.1039/D4NR00321G.

49 W. Y. Teoh, R. Amal and L. Mädler, Flame Spray Pyrolysis: An Enabling Technology for Nanoparticles Design and Fabrication, *Nanoscale*, 2010, **2**(8), 1324, DOI: 10.1039/c0nr00017e.

50 V. Müller, M. Rasp, G. Štefanić, J. Ba, S. Günther, J. Rathousky, M. Niederberger and D. Fattakhova-Rohlfing, Highly Conducting Nanosized Monodispersed Antimony-Doped Tin Oxide Particles Synthesized via Nonaqueous Sol–Gel Procedure, *Chem. Mater.*, 2009, **21**(21), 5229–5236, DOI: 10.1021/cm902189r.

51 J. Kong, H. Deng, P. Yang and J. Chu, Synthesis and Properties of Pure and Antimony-Doped Tin Dioxide Thin Films Fabricated by Sol–Gel Technique on Silicon Wafer, *Mater. Chem. Phys.*, 2009, **114**(2–3), 854–859, DOI: 10.1016/j.matchemphys.2008.10.049.

52 K. Peters, P. Zeller, G. Stefanic, V. Skoromets, H. Němec, P. Kužel and D. Fattakhova-Rohlfing, Water-Dispersible Small Monodisperse Electrically Conducting Antimony Doped Tin Oxide Nanoparticles, *Chem. Mater.*, 2015, **27**(3), 1090–1099, DOI: 10.1021/cm504409k.

53 D. Chen, X. Liu, J. Han, M. Jiang, Y. Xu and M. Xu, Measurements of Particulate Matter Concentration by the Light Scattering Method: Optimization of the Detection Angle, *Fuel Process. Technol.*, 2018, **179**, 124–134, DOI: 10.1016/j.fuproc.2018.06.016.

54 B. García-Cámara, J. M. Saiz, F. González and F. Moreno, Nanoparticles with Unconventional Scattering Properties: Size Effects, *Opt. Commun.*, 2010, **283**(3), 490–496, DOI: 10.1016/j.optcom.2009.10.027.